Revista de la Academia Colombiana de Ciencias Exactas, Físicas y Naturales. 2026
doi: https://doi.org/10.18257/raccefyn.4046

Physical Sciences

Original article

Effects of rare-earth and Ca substitution on the structural and electronic properties of *RE*$Ba_{1.9}Ca_{0.1}Cu_3O_{7-\delta}$ superconductors

Efectos de la sustitución de tierras raras y Ca sobre las propiedades estructurales y electrónicas de los superconductores *RE*$Ba_{1.9}Ca_{0.1}Cu_3O_{7-\delta}$

Cesar Camilo Canaria-Camargo[1], Indry Milena Saavedra-Gaona[1], Sebastian Amaya-Roncancio[1], Agueda María Turatti[2], Jorge Luiz Pimentel-Junior[2], Carlos Arturo Parra-Vargas[1,*], David Arsenio Landinez-Tellez[3]

[1] Grupo de Física de Materiales, Escuela de Física, Universidad Pedagógica y Tecnológica de Colombia, Tunja, Colombia
[2] Instituto de Matemática, Estatística e Física, Universidade Federal Do Rio Grande, Rio Grande do Sul, Brazil
[3] Grupo de Física de Nuevos Materiales, Departamento de Física, Universidad Nacional de Colombia, Bogotá, Colombia

Abstract

We present a combined theoretical and experimental investigation of the structural, energetic, and electronic properties of *RE*$Ba_{1.9}Ca_{0.1}Cu_3O_{7-\delta}$ (*RE*Ba1.9) superconducting systems, where *RE* = Ho, Dy, Gd, and Sm. Calculations based on density functional theory (DFT) revealed that lattice parameters decreased systematically as *RE* ionic radii decreased, consistent with structural contraction. All compounds exhibited negative formation energies, confirming their thermodynamic stability. RE^{3+} substitutions were energetically favorable, particularly for heavier rare-earth elements, thereby enhancing lattice stabilization. Partial $Ba^{2+} \rightarrow Ca^{2+}$ substitution was also energetically viable and preserved structural integrity, whereas full substitution turned unfavorable due to increased lattice strain. The density of states (DOS) analysis showed that Ca incorporation modified the electronic structure by introducing Ca-*d* states near the Fermi level, potentially influencing superconducting behavior. Experimentally, *RE* and Ca substitutions strongly influenced critical superconducting parameters such as the critical current density (J_c), the coherence length (ξ_c), and the magnetic penetration depth (λ_{ab}) due to modified microstructures and vortex pinning mechanisms. The upper critical field $H_{c2}(T)$, estimated via Hao–Clem and two-fluid model fits, showed a clear enhancement with partial Ca doping and *RE* substitution. This increase in $H_{c2}(0)$ suggests an enhanced tolerance to external magnetic fields and improved superconducting stability. The reduced critical-field-density $H_{c2}(0)/T_{c0}$ was notably higher in Sm-based compounds, confirming their enhanced superconducting performance under applied fields.

Keywords: $REBa_2Cu_3O_7$, critical fields (H_{c1}, H_{c2}), current density (J), penetration depth (λ), coherence length (ξ), calcium doping, high-T_c superconductors.

Resumen

Se presenta aquí una investigación combinada, teórica y experimental, de las propiedades estructurales, energéticas y electrónicas de sistemas superconductores *RE*$Ba_{1.9}Ca_{0.1}Cu_3O_{7-\delta}$ (*RE*Ba1.9), donde RE = Ho, Dy, Gd y Sm. Los cálculos basados en la teoría del funcional de la densidad (DFT) revelaron que los parámetros de red disminuyeron sistemáticamente al reducirse el radio iónico del elemento de tierras raras, lo que se ajustó a la contracción estructural esperada. Todos los compuestos presentaron energías de formación negativas, lo que confirmó su estabilidad termodinámica. Las sustituciones de RE^{3+} fueron energéticamente favorables, especialmente para los elementos de tierras raras más pesados, contribuyendo así a una mayor estabilización de la red cristalina. La sustitución parcial de Ba^{2+} por Ca^{2+} también resultó energéticamente viable y preservó la integridad estructural, en tanto que la sustitución total se tornó desfavorable debido al aumento de la deformación de la red.

Citation: Canaria-Camargo CC, et al. Effects of rare-earth and Ca substitution on the structural and electronic properties of *RE*$Ba_{1.9}Ca_{0.1}Cu_3O_{7-\delta}$ superconductors. Revista de la Academia Colombiana de Ciencias Exactas, Físicas y Naturales. 2026 July 8. doi: https://doi.org/10.18257/raccefyn.4046

Editor: Rafael González Hernández

***Corresponding autor:**
Carlos A. Parra Vargas;
carlos.parra@uptc.edu.co

Received: February 10, 2026
Accepted: May 5, 2026
Published on line: July 8, 2026

Revista de la Academia Colombiana de Ciencias Exactas, Físicas y Naturales. 2026
doi: https://doi.org/10.18257/raccefyn.4046

El análisis de la densidad de estados (DOS) evidenció que la incorporación de Ca modificó la estructura electrónica al introducir estados Ca-d cerca del nivel de Fermi, lo que puede influir en el comportamiento superconductor. Experimentalmente, las sustituciones de RE y Ca influyeron de manera significativa en parámetros superconductores críticos como la densidad de corriente crítica (J_c), la longitud de coherencia (ξ_c) y la profundidad de penetración magnética (λ_{ab}), debido a microestructuras modificadas y a mecanismos de anclaje de vórtices. El campo crítico superior $H_{c2}(T)$, estimado mediante ajustes con el modelo de Hao–Clem y el modelo de dos fluidos, mostró una clara mejora con el dopaje parcial con Ca y la sustitución de RE. Este aumento de $H_{c2}(0)$ sugiere una mayor tolerancia a campos magnéticos externos y una mejor estabilidad superconductora. El campo crítico reducido $H_{c2}(0)/T_{c0}$ fue notablemente mayor en los compuestos basados en Sm, lo que confirmó su mejor desempeño superconductor bajo campos aplicados.

Palabras claves: $REBa_2Cu_3O_7$, campos críticos (H_{c1}, H_{c2}), densidad de corriente (J), profundidad de penetración (λ), longitud de coherencia (ξ), dopaje de calcio, superconductores de alta T_c.

Introduction

The lower critical field, H_{c1}, represents one of the key parameters in describing the mixed state in type II superconductors. Its experimental determination is usually relatively straightforward, as it manifests itself as an abrupt change in magnetization when transitioning from the Meissner regime to the reversible behavior characteristic of the mixed state, at least in ideal superconductors. This field is closely linked to the free energy associated with a flux line and provides relevant information on fundamental properties such as the penetration depth, λ, and the Ginzburg-Landau parameter, κ (**Tinkham**, 2004). By measuring H_{c1} together with the upper critical field, H_{c2}, which is directly related to the coherence length, ξ, a comprehensive characterization of the parameters describing the mixed state of the superconductor is obtained (**Maki & Beal-Monod**, 1997).

In recent years, significant progress has been made in the development of superconducting materials such as $RE Ba_2Cu_3O_y$ (*RE*-123), where *RE* can be Nd, Sm, Gd, and Dy, among others. Several fundamental challenges have been successfully addressed, focusing on optimizing both the magnetic flux retention and the mechanical strength of these compounds. In parallel, a production-scale process has been implemented by synthesizing *RE*-123 pellets in air or Ar with 1% O_2 atmospheres, using innovative seeds in the form of thin films of Nd_3O deposited on MgO crystals, which has improved the reproducibility and growth efficiency of these materials (**Muralidhar *et al.***, 2010).

In cuprate superconductors, the pronounced two-dimensional (2D) nature of their electronic structure, along with the low superfluid density, favors the emergence of a vortex liquid phase that lies between the vortex solid phase (below $H_{vs}(T)$) and the normal state (above $H_{c2}(T)$ (**Grissonnanche *et al.***, 2014). Here, $H_{vs}(T)$ refers to the vortex solid melting field, the boundary separating the solid vortex phase, where vortices are pinned and ordered, from the vortex liquid phase, where thermal fluctuations lead to vortex motion and dissipation. It has been proposed that, in the underdoped regime, this vortex liquid phase can extend even down to zero temperature ($T = 0$) (**Riggs S. *et al.***, 2011), implying an extended region in the phase diagram with no true long-range vortex order. Despite various measurements, a clear and direct observation of the upper critical field H_{c2} i in these systems remains elusive. For example, superconducting signals have been detected via the Nernst effect (**Wang Y.**, 2003) and magnetization measurements (**Gu *et al.***, 2010) at high magnetic fields, yet there remains uncertainty as to whether these signals originate from vortex excitations below H_{c2} or from superconducting fluctuations above this critical field (**Koshelev**, 1994).

Thus, exploring superconducting fluctuations is essential for precisely identifying critical fields, particularly H_{c1}, which signals the onset of magnetic flux penetration into the superconductor. This parameter offers key insights into the nature and robustness of the superconducting state (**Sarıtekin *et al.***, 2016).

From a computational perspective, the study of superconducting materials such as Y-123 allows us to explore in greater detail how chemical and structural modifications influence their fundamental electronic properties (**Zhang & Xu**, 2020). In particular, calcium (Ca) doping at the barium (Ba) site has been extensively investigated experimentally due to its effect on the critical temperature (T_c), carrier content, and structural stability. However, the electronic mechanism underlying these changes is not fully understood.

In this context, we combined experimental and computational approaches. On the theoretical side, we performed first-principles calculations to analyze two key aspects: (1) the electronic density of states (DOS), which reveals the availability of energy levels near the Fermi level, and (2) the impact of Ca doping on the electronic structure and superconducting parameters. These calculations allowed us to explore how subtle chemical substitutions affect the crystal structure and electronic behavior, offering insights into the tuning of superconducting properties in *RE*-123 systems.

Our results showed that rare-earth substitution, combined with carefully controlled Ca doping, significantly enhanced the thermodynamic, structural, and functional characteristics of high-T_c cuprates. This approach is a promising route for optimizing next-generation superconducting materials.

Experimental details

The superconductor samples REBa$_{1.9}$Ca$_{0.1}$Cu$_3$O$_{7-\delta}$ (REBa1.9), with RE = Ho, Dy, Gd, and Sm, were synthesized using the solid-state reaction (SSR) method, as described in the study by **Camargo *et al.*** (2025). The sintering temperatures varied among the four samples depending on the RE and the ionic radius of the RE^{3+} ion (**Table 1**).

X-ray diffraction (XRD) patterns taken at room temperature were used to identify the crystalline structure of the four samples. The XRD pattern was obtained using a Panalytical X'pert PRO-MPD instrument with an ultrafast X'Celerator detector in a Bragg-Brentano configuration, employing CuKα radiation (λ = 1.5418 Å). The XRD patterns were analyzed with the General Structure Analysis System (GSAS) software.

Formation energies, intercalation energies, and density of states for the different REBa1.9 compounds were calculated through density functional theory using the Quantum-ESPRESSO package (**Giannozzi *et al.***, 2009). The electron–ion interaction was described by ultrasoft pseudopotentials generated using the Rappe–Rabe–Kaxiras–Joannopoulos method (PSlibrary - QuantumESPRESSO, https://pseudopotentials.quantum-espresso.org/legacy_tables). The van der Waals interactions were estimated using the DFT-D3 semiempirical method (**Grimme *et al.***, 2010). The cutoff energy that we chose was 60 Ry for all atoms involved. We implemented the DFT+U (U for Cu 3*d* of 7.0 eV). The threshold for self-consistency was 1×10−5 Ry. Brillouin zone integration was defined in 4×4×12 k-points. For the calculations of variable cell relaxation, we used the quasi-Newton Broyden-Fletcher-Goldfarb-Shanno algorithm until the forces on each atom were less than 10^{-3} eV Å^{-1} and the energy difference between consecutive steps was less than 10^{-6} eV. In every REBa1.9 calculation, all the atoms were free to relax. All molecular and density plots were made with the VESTA package (**Momma & Izumi**, 2011). The formation energy (E_f) was calculated using the equation

$$E_f = E_{REBa1.9} - nE_{RE} - mE_{Ba} - lE_{Ca} - pE_{Cu} - qE_{O} \quad (1),$$

where $E_{REBa1.9}$ is the total energy of all the compound after geometry, relaxation, nE_{RE} is the energy of the n RE atoms, mE_{Ba} is the energy of the m Ba atoms, lE_{Ca} is the energy of the l Ca atoms, pE_{Cu} is the energy of the p isolated Cu atoms, and qE_{O} is the energy of the q isolated O atoms. The energy required to substitute a Ba for a Ca atom was calculated using the replacement energy (E_{int}) as described by the equation

$$E_r = E_{REBa1.9} - E_{RE-123} - nE_{Ca} + mE_{Ba} \quad (2)$$

Revista de la Academia Colombiana de Ciencias Exactas, Físicas y Naturales. 2026
doi: https://doi.org/10.18257/raccefyn.4046

Table 1. Calcination and sintering temperatures of the $REBa_{1.9}Ca_{0.1}Cu_3O_{7-\delta}$ (RE = Ho, Dy, Gd, and Sm) compounds

Sample	Calcination temperature (°C)	Sintering temperature (°C)
HoBa1.9	840	915
DyBa1.9	840	905
GdBa1.9	840	900
SmBa1.9	840	870

where $E_{REBa1.9}$ is the total energy of the system after the substitution of the Ba atom for Ca, E_{RE-123} is the total energy of the system before the substitution, nE_{Ca} is the energy of the n Ca atoms that were introduced to the system, and mE_{Ba} is the energy of the m Ba atoms extracted from the system (**Ziemke *et al.***, 2025). The morphological properties of the compounds were evaluated by SEM using a JSM 6610-LV JEOL equipment. Magnetization measurements as a function of temperature were taken with a Quantum Design Versalab magnetometer for a temperature range of 50–300 K, with the zero field cooled/field cooled (ZFC/FC) method in several applied fields.

Results and discussion

Structural analysis

Figure 1A shows the XRD patterns of each *RE* ion element in the *RE*Ba1.9 system, synthesized using the SSR method. These patterns were compared with the theoretical pattern of the *RE*-123 phase. The Miller indices (*hkl*) of this phase, corresponding to the orthorhombic space group *Pmmm* (47), are also shown. We expected differences in synthesis temperatures based on previous studies that have demonstrated that the crystallization temperatures of *RE*-123 compounds vary depending on the ionic radius of the substituting RE^{3+} ion (**Saavedra-Gaona *et al.***, 2020; **Topal & Akdogan**, 2012). The XRD peak positions remained unchanged for the samples prepared, suggesting that no orthorhombic to tetragonal structural phase transition occurred in *RE*Ba1.9. A reflection at $2\theta = 29.79°$ was identified and marked with the symbol (♦), corresponding to the non-superconducting $BaCuO_2$ phase with cubic symmetry and space group *Im-3m* (229). This phase is typically formed during the thermal processes involved in the SSR route. Its presence is attributed to the absence of the RE^{3+} substituent in certain structural planes and to the limited inherent atomic interdiffusion (**Pinmangkorn *et al.***, 2020; **Wang *et al.***, 2025)we tried to improve the superconducting performance of bulk YBa2Cu3Oy (Y123. The absence of peaks associated with Ca-containing secondary phases indicates that calcium was successfully incorporated into the *RE*Ba1.9 crystal lattice. While Ca predominantly substitutes at the Ba site, there is a considerable possibility of partial substitution at the RE^{3+} site, due to the multiple oxidation states that calcium can exhibit. To confirm the crystal structure and quantify the phase composition of the samples, the XRD patterns were refined using the Rietveld method with the GSAS software. The refined patterns for *RE*Ba1.9 are shown in **Figure 1 B-C**. In these graphs, the experimental pattern is indicated by the symbol (•), the calculated pattern is shown as a cyan line, the background as a pink line, the difference between the experimental and calculated data as a yellow line, and the Bragg positions of the identified phases are represented by vertical bars.

The agreement between the theoretical and experimental profiles confirmed that all samples crystallized in an orthorhombic structure with *Pmmm* (47) symmetry, corresponding to a superconducting phase. This was further supported by the low reliability factors obtained from the refinements (χ^2 and $R(F^2)$). The results indicated that the crystal structure was preserved when the Y atom was substituted with trivalent RE^{3+} ions. The *a*, *b*, and *c* lattice parameters shown in **Figure 1D** increased with larger ionic radii, along with

the unit cell volume, as observed in the magnified view of the main XRD peak (**Figure 1A**, inset). All XRD patterns exhibited a shift toward lower angles as the ionic radius of the *RE* element increased (with coordination number VIII: Ho^{3+} = 1.015 Å, Dy^{3+} = 1.027 Å, Gd^{3+} = 1.053 Å, and Sm^{3+} = 1.079 Å). No diffraction peaks corresponding to Ca-containing secondary phases were detected, indicating that Ca was incorporated into the *RE*-123 lattice structure. Although Ca^{2+} (0.99 Å) primarily substitutes at the Ba^{2+} (1.42Å) site, there is a high probability that it also substitutes at the RE^{3+} site due to the multiple oxidation states of Ca (**Laval & Orlova**, 2002).

The phase content W (%) showed values of 9.8% and 10.9% for the $BaCuO_2$ phase in the HoBa1.9 and DyBa1.9 samples, respectively. The structural anisotropy percentage of the *RE*Ba1.9 samples was calculated using the relation $(\Delta = 100(b - a))/[0.5(b + a)]$, as shown in **Table 2**. These results indicate that, although there are changes in the lattice parameters a and b, the structural anisotropy of the *RE*Ba1.9 compounds decreases as the ionic radius of the *RE* element increases, exhibiting high planar anisotropy with $a \ll c$.

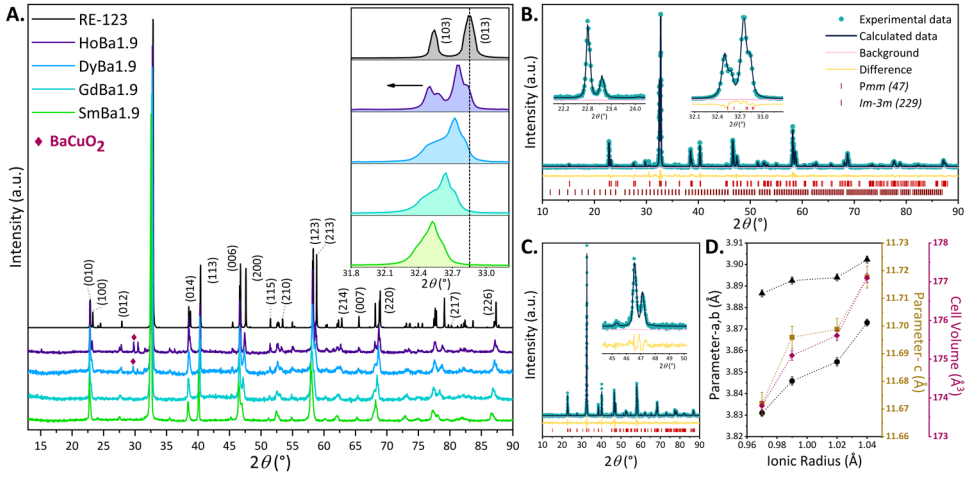

Figure 1. (A) Measured XRD pattern for the $REBa_{1.9}Ca_{0.1}Cu_3O_{7-\delta}$ superconductor as a function of the incidence angle 2θ. The inset shows a zoomed view of the 2θ range [31°, 33°]. Peaks corresponding to the theoretical 123 phase with space group Pmmm (47) are indicated. Rietveld refinement results for samples **(B)** HoBa1.9 and **(C)** GdBa1.9. **(D)** Dependence of lattice parameters (a, b, and c) and unit cell volume on the ionic radius

Table 2. Structural parameters, phase content, orthorhombicity, and reliability factors obtained from the Rietveld refinement

Sample	Phase	Lattice parameters			Cell volume	Cristallite size	Phase content	Anisotropy	c/a ratio	Reliability parameters	
		a (Å)	*b* (Å)	*c* (Å)	(Å³)	*nm*	W (%)	Δ=(100(b-a))/(0.5(b+a))		χ^2	R(F²)
HoBa1.9	Ho-123	3.831(1)	3.886(6)	11.672(1)	173.796(7)	50.3±20.4	90.2	1.44	3.047	1.41(1)	0.131(1)
	$BaCuO_2$	18.850 (5)					9.8				
DyBa1.9	Dy-123	3.845(9)	3.892(5)	11.695(9)	175.097(4)	54.6±37.6	89.1	1.204	3.041	1.34(5)	0.100(1)
	$BaCuO_2$	18.452(3)					10.9				
GdBa1.9	Gd-123	3.854(8)	3.894(1)	11.698(8)	175.612(9)	65.1 ± 46.3	100	1.011	3.035	1.35(7)	0.097(2)
SmBa1.9	Sm-123	3.873(1)	3.902(3)	11.717(7)	177.100(2)	56.9 ± 25.9	100	0.753	3.025	1.36(9)	0.041(8)

Revista de la Academia Colombiana de Ciencias Exactas, Físicas y Naturales. 2026
doi: https://doi.org/10.18257/raccefyn.4046

This suggests a correlation between the RE^{3+} ionic size and the structural symmetry of the system, possibly due to a more uniform accommodation of the crystal lattice as the ionic radius increases.

The crystallite size of all obtained samples was determined using the Scherrer equation: $L = \kappa\lambda/\beta \cos\theta$ where λ is the wavelength of the incident beam, β is the full width at half maximum (FWHM), θ is the Bragg angle of the most intense peak, and κ is the shape factor, taken as 0.9 (**Fatimah *et al.***, 2022). The results in **Table 2** indicate that variations in the ionic radii led to changes in bond distances, which are reflected in the formation of crystallites of different sizes, as well as slight modifications in peak broadening.

Electronic structure analysis

Figure 2 shows the three structures, *RE*-123, *RE*Ba1.9, and *RE*Ca-123, studied to determine the energies of *RE* and Ca in the *RE*-123-type structure. The calculated lattice parameters for the *RE*-123 superconductors (*RE* = Sm, Ho, Gd, Dy) revealed a variation consistent with ionic radius changes of the rare-earth ions. The parameter *a* decreased progressively from Sm-123, with a lattice parameter a calculated at 3.8451 Å, to Ho-123, with a lattice parameter a calculated at 3.7998 Å, correlated with the decreasing ionic radius from Sm to Ho. A similar trend was seen for parameter *b*, from 3.9477 Å for Sm to 3.9277 Å for Ho. The *c* lattice constant exhibited a slight but consistent reduction, from 11.790 Å for Sm to 11.7474 Å for Ho. The reduction in lattice parameters was consistent for all the materials studied compared with the Sm case (**Table 3**). The parameters calculated were in good agreement with the experimental values reported for Ho, Gd, Dy, and Sm.

The formation energy for all the involved Sm-123 species calculated from Eq. 1 is presented in **Table 3**. The calculated E_f value was -5.64 eV per atom, while for SmBa1.9 and SmCa-123, the formation energies were -5.64 eV and -5.53 eV, respectively. These results evidenced that the three systems studied remained energetically stable but that the high values of Ca replacements, as in the case of SmCa-123, were not as energetically favorable as SmBa1.9. The replacement energy E_r calculated from Eq. 2 showed that, for SmBa1.9, replacing one Ba atom with one Ca atom releases 1.18 eV, indicating that the substitution is exothermic. In contrast, for SmCa-123, high Ca contents require 0.69 eV per substituted atom, indicating that extensive Ca substitution is energetically unfavorable because the process is endothermic.

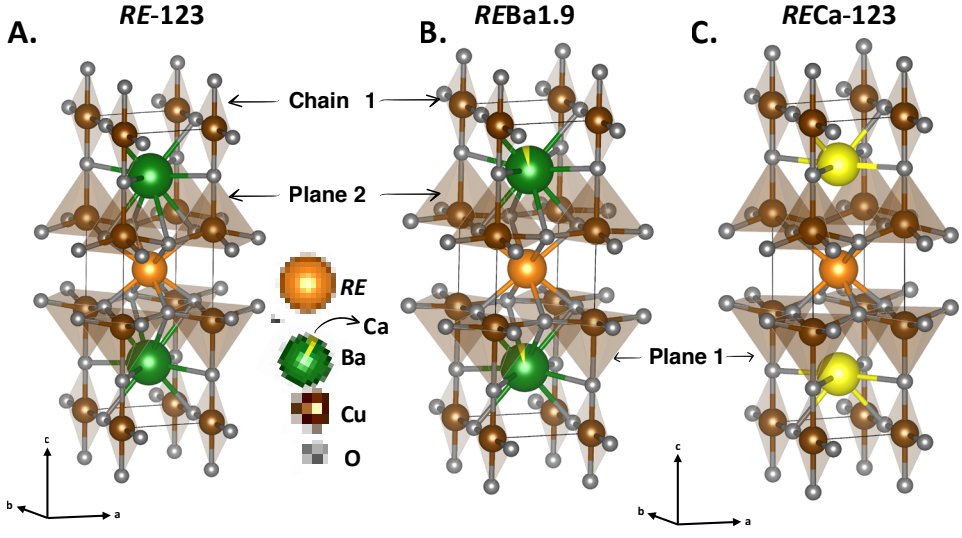

Figure 2. Superconductors unit cells: **(A)** $REBa_2Cu_3O_7$ (RE-123), **(B)** $REBa_{1.9}Ca_{0.1}Cu_3O_7$ (REBa1.9), and **(C)** $RECa_2Cu_3O_7$ (RECa-123), constructed from the refined structural parameters

Table 3. Lattice parameters a, b, c, formation energy E_f, and intercalation energy E_{int} for $REBa_2Cu_3O_7$ (RE-123), $REBa_{1.9}Ca_{0.1}Cu_3O_7$ (REBa1.9), and $RECa_2Cu_3O_7$ (RECa-123) superconductor systems with RE = Ho, Dy, Gd, and Sm

System	Lattice vectors			Formation energy	Replacement energy	
	a	*b*	*c*	E_f / *atom* (eV/atom)	E_r / *atom* (eV/atom)	
$HoBa_2Cu_3O_7$	3.7998	3.9277	11.7474	-5.64	Sm → Ho	-0.11
$DyBa_2Cu_3O_7$	3.8074	3.9327	11.7532	-5.65	Sm → Dy	-0.17
$GdBa_2Cu_3O_7$	3.8261	3.9422	11.7716	-5.65	Sm → Gd	-0.15
$SmBa_2Cu_3O_7$	3.8451	3.9477	11.790	-5.64	--	--
$HoBa_{1.9}Ca_{0.1}Cu_3O_7$	3.831	3.886	11.672	-5.65	Ba→ Ca	-0.21
$DyBa_{1.9}Ca_{0.1}Cu_3O_7$	3.845	3.892	11.695	-5.65	Ba→ Ca	-0.56
$GdBa_{1.9}Ca_{0.1}Cu_3O_7$	3.854	3.894	11.698	-5.66	Ba→ Ca	-1.03
$SmBa_{1.9}Ca_{0.1}Cu_3O_7$	3.873	3.902	11.717	-5.64	Ba→ Ca	-1.18
$HoCa_2Cu_3O_7$	3.5486	3.8602	11.5757	-5.55	Sm → Ho	-0.33
					Ba→ Ca	0.58
$DyCa_2Cu_3O_7$	3.5538	3.8693	11.5625	-5.56	Sm→ Dy	-0.36
					Ba→ Ca	0.59
$GdCa_2Cu_3O_7$	3.5685	3.8874	11.5687	-5.55	Sm → Gd	-0.24
					Ba→ Ca	0.64
$SmCa_2Cu_3O_7$	3.581	3.9092	11.556	-5.53	--	--
					Ba→ Ca	0.69

For Ho-123, the formation energy was calculated at -5.64 eV, and the replacement energy of the Sm→Ho process was an exothermic process, giving -0.11 eV per atom to the system. The HoBa1.9 remained stable, with a formation energy of 5.65 eV per atom, while the Ba→Ca substitution energy was calculated at -0.21 eV. In this case, if the amount of Ca replaced into the structure is increased, the replacement energy becomes positive, showing the endothermic nature of replacing high CA values, with a calculated value of 0.58 eV per atom.

Gd-123 had an E_f (calculated with Eq. 1) of -5.65 eV; the replacement of an Sm atom with a Gd one was calculated at -0.24 eV. On the other hand, for GdBa1.9 and GdCa-123, the formation energy was -5.65 eV and -5.55 eV, respectively. As in other cases, the high amount of Ca in the structure is less energetically favorable. The replacement energy of Ba→Ca in GdBa1.9 was calculated at -1.03 eV, while for GdCa-123, the energy was 0.64 eV. Again, the calculated energies suggested that Ca incorporation in the structure may be energetically favorable, in agreement with the experimental formulation. For Dy-123, DyBa1.9, and DyCa-123, the formation energy was calculated at -5.64 eV, -5.65 eV, and 5.56 eV per atom, respectively. The replacement energy of Ba→Ca in the $DyBa_{1.9}Ca_{0.1}Cu_3O_7$ was calculated at -0.56 eV, while for DyCa-123, the replacement energy was calculated at 0.59 eV per atom. As in the other cases, the calculations predicted that for the experimental proportions to be energetically favorable and the high amounts of Ca in the structure stable, the substitution of energy from the system is required.

Figure 3 shows the comparative density of states (DOS) analysis for the series of *RE*-123-based superconductors (*RE* = Sm, Eu, Gd, Dy, Ho) and their calcium-substituted

Revista de la Academia Colombiana de Ciencias Exactas, Físicas y Naturales. 2026
doi: https://doi.org/10.18257/raccefyn.4046

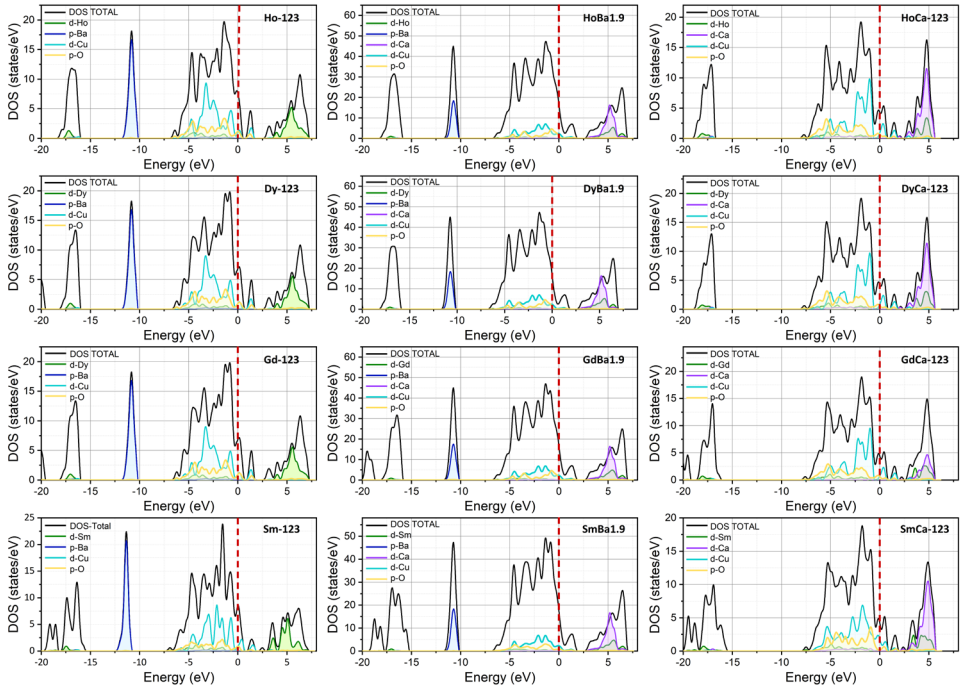

Figure 3. Density of states calculated for $REBa_2Cu_3O_7$ (RE-123), $REBa_{1.9}Ca_{0.1}Cu_3O_7$ (REBa1.9), and $RECa_2Cu_3O_7$ (RECa-123) superconductor systems with RE = Ho, Dy, Gd, and Sm

derivatives. The calculated DOS indicated systematic electronic modifications related to elemental substitution at the Ba site. In all pristine compounds, i.e., with no Ca intercalation, the states below the Fermi level predominantly originate from Cu-3*d* orbitals complemented by significant contributions from O-2*p* orbitals. States above the Fermi energy mainly reflect *RE d*-states and partially Ba-derived orbitals located at higher energies, about 4 eV to 6 eV. Upon gradual Ca substitution, a notable redistribution of electronic states occurs. Here, Ca substitution systematically introduced distinct Ca-*d* states into the higher-energy region, clearly evident between 4 and 6 eV above the Fermi level. Although these Ca-induced states were energetically distant from the Fermi level, their presence markedly altered the local chemical environment, resulting in subtle yet observable shifts in the electronic distribution of Cu-3*d* and O-2*p* orbitals around the Fermi region. Specifically, the progressive increase in Ca content consistently reduced the relative contribution of *RE*-derived states and modified Ba/Ca balance, suggesting structural and electronic alterations that potentially affect superconducting properties indirectly. It was observed that even minor chemical modifications, such as Ba → Ca replacement, induced significant electronic changes that influenced the structural stability, electron-phonon interactions, and ultimately, the superconducting transition characteristics of this high-temperature superconductor family.

Morphological analysis

The micrographs obtained from the secondary electrons shown in **Figure 4** correspond to SEM images of the fractured surfaces of ceramic samples HoBa1.9 **(A)**, DyBa1.9 **(B)**, GdBa1.9 **(C)**, and SmBa1.9 **(D)**. All images were obtained at 1000x magnification, with insets at 3500x to highlight fine morphological details. In micrograph **(A)**, corresponding to the HoBa1.9 sample, relatively dense areas and lamellar surfaces can be observed, suggesting a partially compact microstructure. Some dispersed cavities or pores are visible, as well as regions with trans-granular fracture, indicating a certain degree of grain cohesion. The inset reveals a more detailed surface, with irregular pores and well-defined edges,

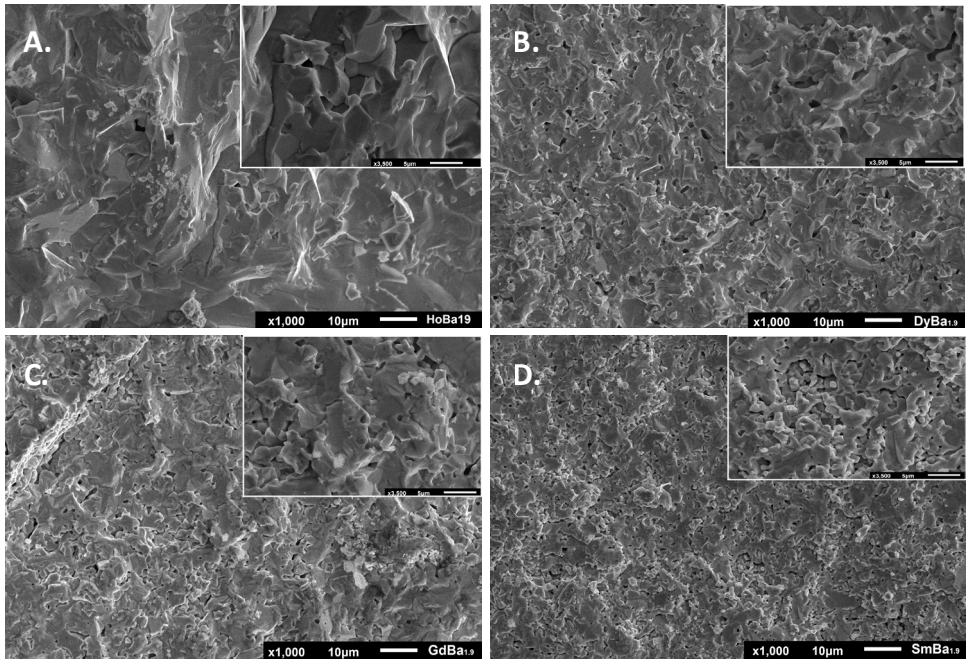

Figure 4. SEM images taken with the secondary electrons of the granule surface of the $REBa_{1.9}Ca_{0.1}Cu_3O_{7-\delta}$ (REBa1.9) superconductors (magnification: 1 k×). There is a 3.5 k micrograph in each inset. **(A)** HoBa1.9, **(B)** DyBa1.9, **(C)** GdBa1.9, and **(D)** SmBa1.9

suggesting incomplete or heterogeneous sintering compared to the other compositions.

In contrast, the micrographs of the DyBa1.9 (B), GdBa1.9 (C), and SmBa1.9 **(D)** samples reveal more porous surfaces and a less dense morphological texture. The DyBa1.9 sample exhibits an open microstructure, with numerous interconnected pores and a homogeneous distribution, indicating a lower degree of sintering. The GdBa1.9 sample shows a rougher surface with high porosity, although some regions of greater densification are observed, which may be attributed to local variations in the thermal process. Finally, the micrograph corresponding to the SmBa1.9 sample reveals a highly porous structure, with rounded and uniformly distributed cavities. These morphological differences highlight how the nature of the rare earth cation influences the final microstructure of the material, affecting both densification and pore connectivity.

The morphology of these materials significantly affected both current flow and magnetic field behavior. In samples with higher porosity and lower densification (DyBa1.9, GdBa1.9, and SmBa1.9), the presence of interconnected pores could have acted as scattering centers and weak links, hindering the continuous flow of charge carriers. This may result in reduced electrical conductivity and a lower critical current density (J_c) (**Salama *et al.***, 1989). Furthermore, the irregular distribution of pores and grain boundary defects can serve as magnetic flux pinning centers, which may either enhance or impair the pinning capability depending on their size and distribution (**Slimani *et al.***, 2019). In contrast, the observed HoBa1.9 sample's more compact and lamellar morphology is likely to promote better grain connectivity and fewer weak links, thus enabling more efficient current transport and potentially improving flux pinning performance (**Matsushita**, 2000). Overall, the microstructural differences induced by the choice of a rare earth cation play a crucial role in the electromagnetic behavior of these materials.

Critical magnetic parameters

Critical temperature (T_c) and irreversibility temperature (T_{irr}). The typical behavior of a superconductor is characterized by the clear presence of T_c, which marks the transition

Revista de la Academia Colombiana de Ciencias Exactas, Físicas y Naturales. 2026
doi: https://doi.org/10.18257/raccefyn.4046

between the normal and superconducting phases, as evidenced by the onset of the diamagnetic response observed below T_c. The T_c values for the *RE*Ba1.9 compounds were determined from the intersection of the extrapolated magnetization curves corresponding to the normal and superconducting phases in the Zero Field Cooling (ZFC) mode (**Figure 1**). The irreversibility temperature (T_{irr}) was determined by accurately identifying the bifurcation point between the ZFC and FC curves (**Figure 5**). This parameter is significant, as it provides information on the stability of the superconducting state against thermal fluctuations. According to the values presented in **Table 4**, the materials studied exhibited Tc values above 30 K and can, therefore, be classified as high-temperature superconductors (HTcS, Type II) (**Sunku Prasad *et al.***, 2019). The T_{irr} is consistently lower than T_c, as expected in high-temperature superconductors, due to the presence of flux creep and thermal fluctuations. Additionally, T_c showed a strong dependence on the ionic radius of the substituent ion RE^{3+}. In this context, T_c increased as the ionic radius of RE^{3+} decreased, a trend that suggests that smaller RE^{3+} ions may induce less structural distortion or favor more efficient charge carrier distribution within the CuO_2 planes, which in turn enhances the superconducting properties.

Based on the ionic radii of Ba^{2+} (1.35 Å) and Ca^{2+} (0.99 Å), the smaller size of Ca^{2+} suggests that it can substitute into the Ba^{2+} site within the crystal lattice. From a charge compensation perspective, both Ca^{2+} and Ba^{2+} are divalent cations, making such a substitution chemically favorable. When Ca^{2+} replaces Ba^{2+}, it acts as a hole dopant and induces the formation of vacancies at Ba^{2+} sites. This substitution reduces the overall positive charge within the unit cell, thereby increasing the hole carrier concentration. As a

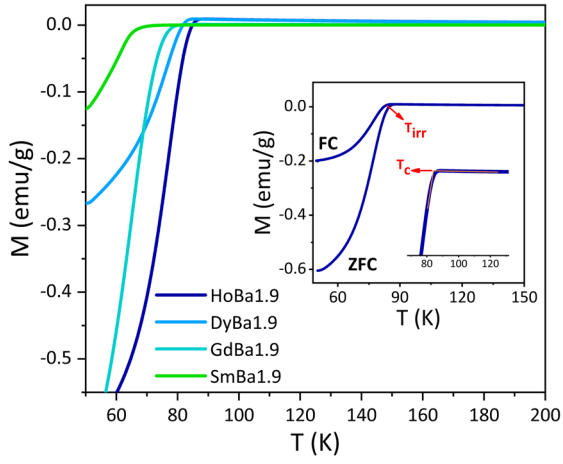

Figure 5. Magnetization curves as a function of temperature in ZFC mode for the $REBa_{1.9}Ca_{0.1}Cu_3O_{7-\delta}$ (REBa1.9) superconductor systems. The inset illustrates the criteria used to determine T_c and T_{irr}.

Table 4. Thermodynamic parameters for $REBa_{1.9}Ca_{0.1}Cu_3O_{7-\delta}$ (REBa1.9) superconductors systems.

System	T_c (K)	T_{c0} (K)	A_S ($\times10^{-9}$) (1/K)	B_{LD} ($\times10^{-3}$)	ξ_{ab} (Å)	ξ_c (Å)	T_{irr} (K)	$\lambda_{ab}(0)$ (Å)	$\xi_{Hc2}(0)$ (Å)	κ	$H_{c1}(0)$ (Oe)	$H_{c2}(0)$ (Oe)	$J_c(0)$ (1×10^6) (A/cm^2)	$H_{c2}(0)/T_{c0}$ (Oe/K)
HoBa1.9	85.75	83.89	5.37	1.19	12.15	1.19	85.51	2390	304.47	7.84	183	3550	5.79	42.31
DyBa1.9	82.42	81.39	5.23	0.95	12.00	0.95	82.36	2460	333.44	7.37	211	2960	4.99	36.36
GdBa1.9	71.57	70.58	6.53	0.85	13.51	0.85	71.27	2840	312.96	9.07	191	3360	3.95	47.60
SmBa1.9	68.06	66.42	10.41	1.63	16.94	1.63	67.75	3120	68.56	45.50	178	70000	15.10	1053.89

consequence, T_c tends to decrease with increasing Ca^{2+} content due to the modification of the charge carrier balance. Furthermore, a decrease in the ionic radius of the *RE* element also leads to a reduction in Tc. This behavior is commonly attributed to increased lattice distortion and modified electronic structure, both of which affect the superconducting properties (**Jin *et al.,*** 2009; **Noudem *et al.***, 2003).

Mid-field transition temperature value (T_{c0}), penetration length (λ_{ab}), and critical current density (J_c). T_{c0} is the mean-field transition temperature, i.e., the temperature at which the material becomes superconducting according to the mean-field model (**Mosqueira *et al.***, 1996). In this model, interactions and thermal fluctuations are assumed to be negligible or minimized. The model is based on theories such as the Bardeen-Cooper-Schrieffer (BCS) theory, or more complex models adapted to the systems analyzed in this study (**van Otterlo *et al.***, 1999). **Figure 6A** shows how we determined the Tc0 value by extrapolating the linear region $-T/\Delta\chi$ to its intersection with the temperature axis. The analysis of the excess diamagnetism ($\Delta\chi$) above T_{c0} was done in terms of thermal fluctuations in the amplitude of the order parameter, characterized by $\xi_{ab}(0)$ and $\xi_c(0)$. Equation 3 represents a quadratic function. When plotting $(-T/\Delta\chi)^2$ as a function of the reduced temperature (ε), a parabolic region was observed for positive values of ε (**Figure 6B**). The data we obtained fit a second-degree polynomial, allowing for the determination of the parameters B_{LD} (Lawrence Doniach parameter) and A_s (Schmidt diamagnetism) (**Table 4**). The inset in **Figure 6B** shows a log-log plot of the excess diamagnetism as a function of temperature, which allows for the determination of the system's dimensionality (x). From the slope of the linear fit, denoted as x, one can infer the dimensionality of the system: $x = -1$, indicating a two-dimensional (2D) regime, while $x = -0.5$ corresponds to a three-dimensional (3D) regime. The extracted values range from −0.97 (for SmBa1.9) to 1.01 (for DyBa1.9) confirmed the two-dimensional nature of the superconducting systems under study.

$$\left(\frac{T}{\Delta\chi}\right)^2 = \frac{1}{4A_s^2}\varepsilon^2 + \frac{B_{LD}}{A_S^2}\varepsilon \tag{3}$$

To determine the coherence length associated with the fluctuation regime in the *ab* planes, $\xi_{ab}(0)$, and along the *c*-axis, $\xi_c(0)$, we used Equation 4 in the MKS system, where ϕ is the magnetic flux quantum, s is the periodicity length of the superconducting CuO_2 layers, and the synthesized samples are orthorhombic with two CuO_2 planes per unit cell, with $s = d_1 + d_2 \approx c$, and K_B is the Boltzmann constant, while μ_0 is the permeability of free space.

$$\xi_{ab}(0) = \sqrt{\frac{3A_s\phi^2 s}{\mu_0 \pi K_B}};\ \xi_c(0) = \frac{s\sqrt{B_{LD}}}{2} \tag{4}.$$

When the magnetic field H is applied perpendicular to the CuO_2 planes, it has a significant effect on the values of the penetration depth, $\lambda_{ab}(T)$, the Ginzburg–Landau (GL) parameter, and the upper critical field H_{c2}. These values can be extracted from reversible magnetization data below T_{c0}. Since $\lambda_{ab}(T)$ varies with temperature, we selected several temperatures below T_{c0} at which $\lambda_{ab}(T)$ can be considered fixed. Based on these values, an extrapolation to T = 0 K was performed, yielding the zero-temperature penetration depth $\lambda_{ab}(0)$. It was evident that ΔM_{ab} exhibited a linear dependence on $Ln(H)$, with a slope given by $\lambda_{ab}(T) = \sqrt{s\phi_0^2/64\pi^2(2s\phi_0 C + k_B T)}$. Therefore, plots of ΔM_{ab} as a function of LnH were constructed for each selected temperature (**Figure 6C**). These isotherms correspond to the reversible magnetization regime. The detailed procedure can be found in **Camargo *et al.*** (2025).

$$\Delta M_{ab} = \left(\frac{\phi_0}{64\pi^2\lambda_{ab}^2(T)} - \frac{k_B T}{2s\phi_0^2}\right) Ln(H) \tag{5}$$

Figure 6D shows the variation in penetration depth with temperature, compared with different theoretical models. The red solid line represents the result from the two-fluid

Revista de la Academia Colombiana de Ciencias Exactas, Físicas y Naturales. 2026
doi: https://doi.org/10.18257/raccefyn.4046

model (Eq. 6), the black solid line corresponds to BCS calculations (Eq. 7), and the blue solid line shows the result from the quadratic model (Eq. 6). In the two-fluid model, λab (0) was treated as a free parameter, and the exponent was fixed at $n = 4$. For the quadratic model, λab (0) was again a free parameter with $n = 2$. In the BCS model, λab (0) was the only fitting parameter. In all cases, the critical temperature T_c had the same value. The fits obtained from each model for the HoBa1.9 sample are also shown. The two-fluid model provided the best agreement with the experimental data, for which we chose it to perform a reliable extrapolation at zero temperature and determine λab (0) for each system.

$$\lambda_{ab}(T) = \frac{\lambda_{ab}(0)}{\left[1 - \left(\frac{T}{T_c}\right)^n\right]^{1/2}} \quad (6),$$

$$\lambda_{ab}(T) = \frac{\lambda_{ab}(0)}{\left[1 - \left(\frac{T}{T_c}\right)^{3-\frac{T}{T_c}}\right]^{1/2}} \quad (7).$$

The contribution of thermal fluctuations of the order parameter to the London term of the magnetization was evaluated to determine the upper critical field $H_{c2}(0)$ (**Vidal *et al.***, 1988), as defined by Equation 8. This expression is a linear function of ΔM_{ab}. To apply this method, the function $y = Ln(\eta H_{c2}/eH)$ was plotted versus $Ln\ H$, and the resulting straight lines were extrapolated to the y-axis, as shown in the inset of **Figure 7A**. From these extrapolations, H_{c2} (T) was easily determined. For all samples, the same value of the parameter $\eta = 1.4$, associated with the vortex lattice structure, was used as proposed in the Hao–Clem theory. The values of

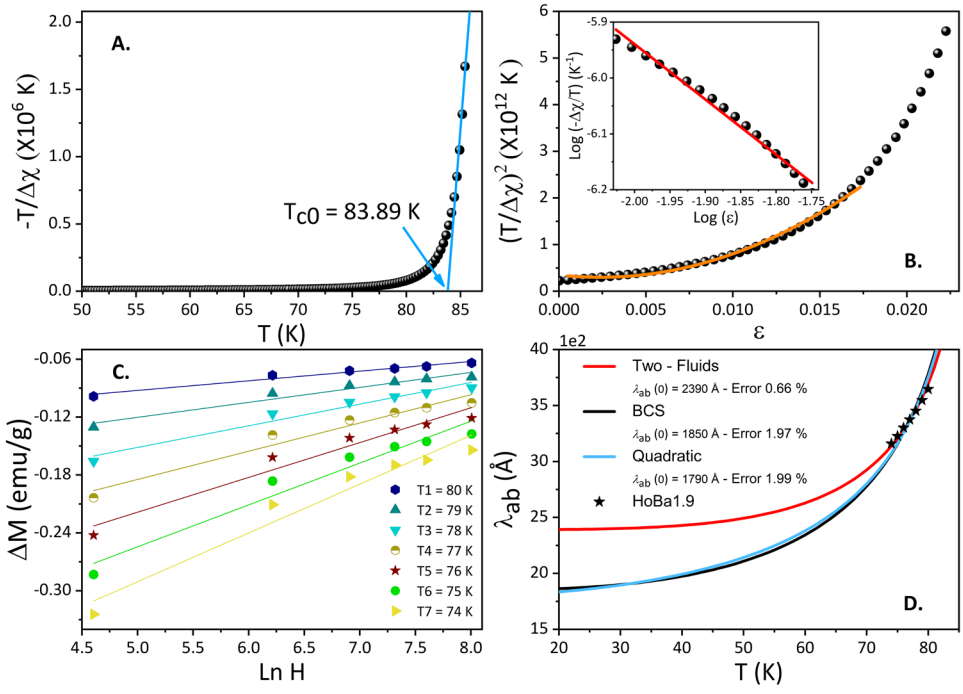

Figure 6. (A) Method used to determine the reduced temperature (T_{c0}). **(B)** Excess diamagnetism as a function of reduced temperature. **(C)** Isotherms of excess magnetization as a function of Ln H in the low-temperature regime (79.2 – 89.5 K). **(D)** Magnetic penetration depth as a function of temperature for the HoBa1.9 superconductor system

H_{c2} (T) were then plotted as a function of temperature, resulting in a straight line with a slope dH_{c2}/dT intercepting the temperature axis near T_{c0}. The value of dH_{c2}/dT allowed us to estimate $H_{c2}(0)$ using Equation 9. By substituting the $H_{c2}(0)$ value into the equation $\xi_{Hc2} = \sqrt{\phi_0/2\pi H_{c2}(0)}$, we calculated the coherence length $\xi_{Hc2}(0)$. The values for each of the systems are presented in **Table 4**.

$$n\frac{\rho H_{c2}}{eH} = -\frac{32\pi^2\lambda_{ab}^2}{\phi_0(1-g)}\Delta M_{ab} + \frac{g}{1-g}Ln\frac{g}{e}; g(T) = \frac{32\pi^2\lambda_{ab}^2 k_B T}{\phi_0^2} \quad (8),$$

$$H_{c2}(0) = 0.7T_{c0}[dH_{c2}/dT]_{\approx T_c} \quad (9).$$

Several studies on the J_c in polycrystalline samples have highlighted the strong granularity of these compounds, which significantly limits the global values to very low levels (**Yamamoto *et al.***, 2008). Using theoretical models, it is possible to calculate the value of J_c, but it must be noted that the superconducting state requires the temperature, magnetic field, and current density to remain below their respective critical parameters; therefore, determining these values is essential. To estimate the order of magnitude of J_c (0), we used Equation 10 (**Shams & Ranjbar**, 2022), taking into account different $\xi_{Hc2}(0)$ and λ_{ab} (0) for each of the synthesized system values (**Table 3**). The order of magnitude of $J_c(0)$ for each of the superconducting samples was approximately 1×10^6 A/cm^2, which is a notably high value for a type-II superconductor, and may be attributed to the high densification of the material, as well as to the epitaxial growth observed in the micrographs. This suggests that the grains and crystals within the material are well-packed and partially biaxially oriented, reducing the void space between them. Such structural improvement resulted in enhanced electrical conductivity and a higher capacity to carry current without resistance. Using the obtained J_c (0) value, it was possible to model the temperature dependence of the critical current density as $J_{c,ab}(0)$. **Figure 7C** shows the critical current

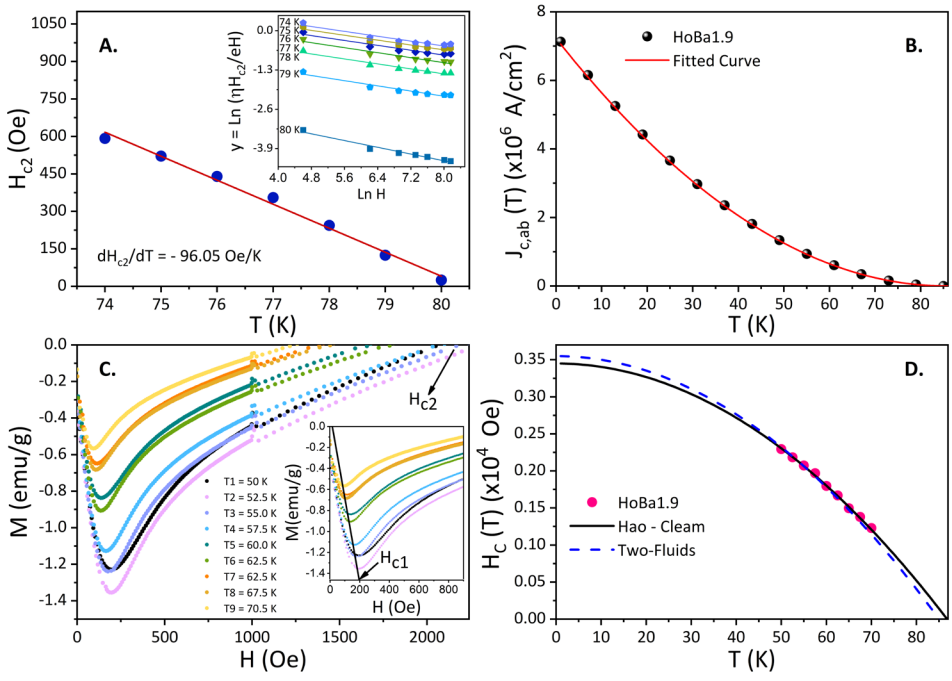

Figure 7. (A) Critical magnetic field (H_{c2}) as a function of temperature (T). **(B)** Critical current density (J_c) versus T curve. **(C)** Hysteresis loops measured at 50 K for different temperatures. **(D)** Thermodynamic critical field (H_c) as a function of T, determined in different ways for the HoBa1.9 superconductor system

Revista de la Academia Colombiana de Ciencias Exactas, Físicas y Naturales. 2026
doi: https://doi.org/10.18257/raccefyn.4046

density as a function of temperature for the polycrystalline HoBa1.9 sample, which was obtained by comparing magnetization data, as described in Equation 11. $J_{c,ab}(0)$ tends to decrease as the temperature approaches T_c. (**Matsushita *et al.***, 2002); this is attributed to the increase in thermal vibrations at higher temperatures, which disrupts the orderly motion of Cooper pairs responsible for superconductivity. As a result, the material's ability to carry electrical current without resistance decreases (**Yamamoto *et al.***, 2008).

$$J_c(0) = \frac{2}{3\sqrt{3}} \frac{\xi_{Hc2}}{\lambda_{ab}^2(0)} H_{c2} \quad (10)$$

$$J_c(T) = J_c(0) \left[1 - \left(\frac{T}{T_c}\right)\right]^2 \quad (11)$$

Critical fields (H_{c1}, H_{c2})

High-temperature superconducting materials exhibit type-II behavior, characterized by the presence of two critical fields, H_{c1} and H_{c2}, as observed in magnetization measurements as a function of an applied magnetic field. Here, we measured at various fixed temperatures in the 50 to 70 K range, while varying the magnetic field between –30 and 30 kOe. H_{c1} and H_{c2} experimental values for the *RE*Ba1.9 samples are presented in **Table 4**. These values were extracted from the magnetization versus applied magnetic field $M(H)$ curves for each superconducting sample (**Figure 7C**). These data indicated that the critical fields H_{c1} and H_{c2} increased as the temperature decreased, suggesting greater stability of the superconducting state at lower temperatures, as reduced thermal vibrations require a stronger magnetic field to suppress superconductivity. According to our results, the synthesized superconducting samples exhibited magnetic field exclusion within the sample (Meissner effect) under low applied magnetic fields, as the H_{c1} values did not exceed 250 Oe. The critical field values H_{c2} (50) were found to lie approximately in the range of 1 to 30 kOe. Furthermore, we observed that both H_{c1} and H_{c2} decreased with increasing temperature. This behavior may be attributed to the weakening of Cooper pairs at higher temperatures due to increased thermal energy, which can break the pairs. Another possible explanation is the loss of magnetic ordering: at elevated temperatures, the alignment of magnetic moments within the material may weaken, leading to greater magnetic field penetration and, consequently, a reduction in the critical fields (**Costa & Pavão**, 2012).

We plotted the experimental data of the upper critical field H_{c2} as a function of temperature for the HoBa1.9 sample and fit them using two theoretical models: the Hao–Clem model and the two-fluid model, to estimate the corresponding thermodynamic critical field curve. As shown in **Figure 7D**, the experimental results displayed good agreement with the Hao–Clem model, with H_{c2} values ranging from 0.36 T at 67.5 K to 3.0 T at 50 K. The data points are represented by solid purple circles. The Hao–Clem model (**Hao *et al.***, 1991) fit is shown as a solid black line and follows a parabolic dependence given in Equation 12. Additionally, the two-fluid model (**Bardeen *et al.***, 1957) is represented by a blue dashed line and follows a similar parabolic dependence (Eq. 13). Both curves were extrapolated to zero temperature to estimate the zero-temperature upper critical field $H_{c2}(0)$.

$$H_c(T) = H_{c2}(0) \left[1 - \left(\frac{T}{T_c}\right)^2\right] (12)$$

$$H_c(T) = H_{c2}(0) \left[1 - \left(\frac{T}{T_{c0}}\right)^2\right] (13)$$

An increase in the value of $H_{c2}(0)$ leads to a corresponding rise in the change in free energy, or condensation energy, as it reflects a greater resistance of the superconducting state to external magnetic fields. This implies that more energy is required to sustain superconductivity, which is manifested in the higher free energy associated with the superconducting phase. The condensation energy reaches its maximum near, in agreement with the theoretical expression $H_{c2}(0)^2 / 8\pi$, which describes the condensation energy

density (**Tinkham**, 2004)this volume emphasizes physical arguments and minimizes theoretical formalism. The second edition of this classic text features revisions by the author that improve its user-friendly qualities, and an introductory survey of latter-day developments in classic superconductivity enhances the volume's value as a reference for researchers. Starting with a historical overview, the text proceeds with an introduction to the electrodynamics of superconductors and presents expositions of the Bardeen-Cooper-Schrieffer theory and the Ginzburg-Landau theory. Additional subjects include magnetic properties of classic type II superconductors; the Josephson effect (both in terms of basic phenomena and applications and of the phenomena unique to small junctions. A strong dependence on the critical temperatures T_c and T_{c0} is observed. **Table 4** presents the ratio $H_{c2}(0)/T_{c0}$, known as the reduced critical field density. In general, this value is significantly higher for the SmBa1.9 system, indicating that these materials are more robust and capable of withstanding stronger magnetic fields at lower temperatures.

The RE^{3+} ions such as Sm^{3+}, Gd^{3+}, Dy^{3+}, and Ho^{3+} along with Ca^{2+} doping in the Y:123 superconductor, influence key critical parameters such as J_c, ξ, and λ. It has been observed that replacing Y with these rare-earth elements alters the microstructure of the material, which in turn affects vortex pinning mechanisms, thereby modifying J_c. The inclusion of Ca^{2+} in the Y:123 lattice can introduce defects and strain in the crystal structure that act as effective vortex pinning centers, enhancing the critical current (**Böhmer *et al.***, 1997). However, excessive Ca^{2+} content may lead to structural disorder, ultimately reducing J_c.

Conclusions

The analysis of the structural, energetic, and electronic properties of the *RE*-123 and *RE*Ba1.9 systems (RE = Sm, Ho, Gd, Dy) revealed clear trends associated with rare-earth and calcium substitution. The lattice parameters decreased systematically with decreasing *RE* ionic radius, reflecting expected structural contraction. All studied compounds exhibited negative formation energies, confirming their thermodynamic stability. Replacement energies for Sm → *RE* substitutions were slightly negative and increasingly favorable with heavier *RE* elements, indicating that these substitutions are energetically possible and can stabilize the lattice. In contrast, Ba → Ca substitution showed dual behavior: while partial substitution *RE*Ba1.9 was energetically favorable with negative replacement energies, full substitution *RE*Ca-123 became energetically costly, as evidenced by positive replacement energies, although the systems remained globally stable. The calculated values from DFT predicted the energetic viability of the experimental stoichiometry with partial Ca incorporation, as it achieved improved stability without introducing significant lattice strain. The complementary DOS analysis showed that Ca substitution altered the unoccupied states by introducing Ca-*d* orbitals between 4 and 6 eV above the Fermi level, modifying the local chemical environment and potentially influencing the superconducting properties through subtle electronic rearrangements. Altogether, the results supported the energetic and structural preference for rare-earth substitution combined with partial Ca doping, as found in experimentally realized high-T_c. From an experimental perspective, the substitution of Y^{3+} by RE^{3+} ions, in combination with Ca^{2+} doping, had a direct impact on critical superconducting parameters. These effects were the product of modifications in the microstructure and vortex pinning mechanisms. *RE* substitution enhanced lattice rigidity and vortex pinning, while moderate Ca content introduced effective strain fields and defects that served as additional pinning centers, thus improving J_c.

However, excessive Ca incorporation may induce disorder, ultimately degrading superconducting performance. Altogether, the results support the energetic, structural, and functional preference for rare-earth substitution combined with partial Ca doping, as observed in experimentally realized high-T_c superconductors. This synergy offers a promising route for optimizing performance through controlled chemical engineering at the atomic scale.

Acknowledgments

This work was funded by MINCIENCIAS (Grant No. 785-2017) and was supported by the Research Directorate at Universidad Pedagógica y Tecnológica de Colombia, under project SGI 3237.

Author contributions

C.C.: Formal analysis, investigation, methodology, supervision, visualization, writing of the original draft, review, and editing. **I.M. SG:** Formal analysis, investigation, methodology, supervision, visualization, writing of the original draft. **S. A-R:** Formal analysis, investigation, writing, review, and editing. **A.M. T.** and **J.L. P Jr:** Resources, supervision, writing, review, and editing. **C.A. PV:** Project administration, resources, supervision, writing, review, and editing. **D.A.L. T:** Methodology, visualization, writing, review, and editing, resources.

Conflicts of interest

The authors declare no conflict of interest.

Data and code availability

Data will be made available on request.

References

Muralidhar, M., Tomita, M., Suzuki, K., Jirsa, M. Fukumoto, Y, Ishihara, A. (2010). A low-cost batch process for high-performance melt-textured GdBaCuO pellets. *Superconductor Science and Technology, 23,* 045033. https://doi.org/10.1088/0953-2048/23/4/045033

Bardeen, J., Cooper, L. N., & Schrieffer, J. R. (1957). Theory of superconductivity. *Physical Review, 108*(5), 1175-1204. https://doi.org/10.1103/PhysRev.108.1175

Böhmer, C., Brandstätter, G., Weber, H. W. (1997). The lower critical field of high-temperature superconductors. *Superconductor Science and Technology, 10*(7A), A1. https://doi.org/10.1088/0953-2048/10/7A/002

Camargo, C. C. C., Saavedra-Gaona, I. M., Landínez-Téllez, D. A., Vargas, C. A. P. (2025). Evaluation of the structural, morphological, and magnetic properties of the RE-358, RE-123, RE-Ca0.1 with RE = Gd and Sm superconductors. *Physica C: Superconductivity and its Applications, 630*, 1354647. https://doi.org/10.1016/j.physc.2025.1354647

Costa, M. B. S. & Pavão, A. C. (2012). Supercondutividade: Um século de desafios e superação. *Revista Brasileira de Ensino de Física, 34*, 2602-2615. https://doi.org/10.1590/S1806-11172012000200017

Fatimah, S., Ragadhita, R., Husaeni, D. F. A., Nandiyanto, A. B. D. (2022). How to Calculate Crystallite Size from X-Ray Diffraction (XRD) using Scherrer Method. *ASEAN Journal of Science and Engineering, 2*(1), Article 1. https://doi.org/10.17509/ajse.v2i1.37647

Giannozzi, P., Baroni, S., Bonini, N., Calandra, M., Car, R., Cavazzoni, C., Ceresoli, D., Chiarotti, G. L., Cococcioni, M., Dabo, I., Dal Corso, A., de Gironcoli, S., Fabris, S., Fratesi, G., Gebauer, R., Gerstmann, U., Gougoussis, C., Kokalj, A., Lazzeri, M., … Wentzcovitch, R. M. (2009). QUANTUM ESPRESSO: A modular and open-source software project for quantum simulations of materials. *Journal of Physics: Condensed Matter, 21*(39), 395502. https://doi.org/10.1088/0953-8984/21/39/395502

Grissonnanche, G., Cyr-Choinière, O., Laliberté, F., René de Cotret, S., Juneau-Fecteau, A., Dufour-Beauséjour, S., Delage, M.-È., LeBoeuf, D., Chang, J., Ramshaw, B. J., Bonn, D. A., Hardy, W. N., Liang, R., Adachi, S., Hussey, N. E., Vignolle, B., Proust, C., Sutherland, M., Krämer, S., … Taillefer, L. (2014). Direct measurement of the upper critical field in cuprate superconductors. *Nature Communications, 5*(1), 3280. https://doi.org/10.1038/ncomms4280

Grimme, S., Antony, J., Ehrlich, S., Krieg, H. (2010). A consistent and accurate ab initio parametrization of density functional dispersion correction (DFT-D) for the 94 elements H-Pu. *The Journal of Chemichal Physics,* 132(15), 154104. https://doi.org/10.1063/1.3382344

Gu, G. D., Li, L., Wang, Y., Komiya, S., Ono, S., Ando, Y., Ong, N. P., Brookhaven National Laboratory (United States). (2010). Diamagnetism and Cooper Pairing Above Tc in Cuprates. *Physical Review. B, Condensed Matter and Materials Physics, 81*(5), 054510.

Hao, Z., Clem, J.R., McElfresh, M.W., Civale, L., Malozemoff, A.P., Holtzberg, F. (1991). Model for the reversible magnetization of high- kappa type-II superconductors: Application to high-Tc superconductors. *Physical Review B Condensed Matter, 43*(4), 2844-2852. https://doi.org/10.1103/physrevb.43.2844. PMID: 9997583

Jin, W., Hao, S., Zhang, H. (2009). The fixed triangle chemical bond and its effect in the Y1−xCaxBa2−yLayCu3Oz system from underdoped to overdoped. *New Journal of Physics, 11*(11), 113036. https://doi.org/10.1088/1367-2630/11/11/113036

Koshelev, A. E. (1994). Ginzburg-Landau theory of fluctuation magnetization of two-dimensional superconductors. *Physical Review B, 50*(1), 506-516. https://doi.org/10.1103/PhysRevB.50.506

Laval, J. & Orlova, T. (2002). Microstructure and superconducting properties of sintered DyBaCuO ceramics doped by Ca. *Superconductor Science and Technology, 15,* 1244. https://doi.org/10.1088/0953-2048/15/8/314

Maki, K. & Beal-Monod, M. T. (1997). Ginzburg-Landau equation and the upper critical field in anisotropic (d+s)-wave superconductivity. *Physical Review B, 55*(17), 11730-11734. https://doi.org/10.1103/PhysRevB.55.11730

Matsushita, T. (2000). Flux pinning in superconducting 123 materials. *Superconductor Science and Technology, 13,* 730. https://doi.org/10.1088/0953-2048/13/6/320

Matsushita, T., Wada, H., Kiss, T., Inoue, M., Iijima, Y., Kakimoto, K., Saitoh, T., Shiohara, Y. (2002). Critical current properties in superconducting Y-123 tapes. *Physica C: Superconductivity, 378-381*, 1102-1107. https://doi.org/10.1016/S0921-4534(02)01718-5

Momma, K. & Izumi, F. (2011). VESTA 3 for three-dimensional visualization of crystal, volumetric and morphology data. *Journal of Applied Crystallography, 44*(6), 1272-1276. https://doi.org/10.1107/S0021889811038970

Mosqueira, J., Miramontes, E. G., Torrón, C., Campá, J. A., Rasines, I., Vidal, F. (1996). Thermal fluctuation effects on the magnetization above and below the superconducting transition in crystals in the weak magnetic field limit. *Physical Review B, 53*(22), 15272-15280. https://doi.org/10.1103/PhysRevB.53.15272

Noudem, J. G., Reddy, E. S., Schmitz, G. J. (2003). Magnetic and transport properties of YBa2Cu3Oy superconductor foams. *Physica C: Superconductivity, 390*(4), 286-290. https://doi.org/10.1016/S0921-4534(03)00755-X

Pinmangkorn, S., Miryala, M., Arvapalli, S. S., Murakami, M. (2020). Effect of Ultra-sonicated Y2BaCuO5 on Top-Seeded Melt Growth YBa2Cu3Oy Bulk Superconductor. *Journal of Superconductivity and Novel Magnetism, 33*(6), 1667-1673. https://doi.org/10.1007/s10948-019-05405-0

Riggs S., Vafek, O., Kemper, J.B., Betts,J.B., Migliori, A., Balakirev, .F., Hardy, W.N., Liang, R., Bonn, D.A., Boebinger, G.S. (2011). Heat capacity through the magnetic-field-induced resistive transition in an underdoped high-temperature superconductor. *Nature Physics, 7*, 332-335 (2011). https://doi.org/10.1038/nphys1921)

Saavedra-Gaona, I. M., Supelano, G. I., Parra-Vargas, C. A. (2020). Determination of critical superconducting parameters based on the study of the magnetization fluctuations for RE3Ba5Cu8O18-δ (RE= Sm, Eu, Gd, Dy and Ho) ceramic superconductor system. *Ceramics International, 46*(8, Part B), 11530-11538. https://doi.org/10.1016/j.ceramint.2020.01.179

Salama, K., Selvamanickam, V., Gao, L., Sun, K. (1989). High current density in bulk $YBa_2Cu_3O_x$ superconductor. *Applied Physics Letters,n54*, 2352-2354. https://doi.org/10.1063/1.101525

Sarıtekin, N. K., Dogruer, M., Zalaoglu, Y., Yıldırım, G., Terzioglu, C., Gorur, O. (2016). Filling of electronic density of states in Y-123 superconducting ceramics by nano Nd substitution on Ba site in crystal structure. *Journal of Alloys and Compounds, 659*, 31-37. https://doi.org/10.1016/j.jallcom.2015.10.295

Shams, G. & Ranjbar, M. (2022). Phase diagram of high temperature $Y_1Ba_2Cu_3O_{7-\delta}$ superconductor by Bean's model and experimental techniques. *Bulletin of Materials Sciences, 45*, 206. https://doi.org/10.1007/s12034-022-02796-0

Slimani, Y., Almessiere, M. A., Hannachi, E., Baykal, A., Manikandan, A., Mumtaz, M., Ben Azzouz, F. (2019). Influence of WO3 nanowires on structural, morphological and flux pinning ability of YBa2Cu3Oy superconductor. *Ceramics International, 45*(2, Part A), 2621-2628. https://doi.org/10.1016/j.ceramint.2018.10.201

Sunku Prasad, J., Muthukumar, P., Desai, F., Basu, D. N., Rahman, M. M. (2019). A critical review of high-temperature reversible thermochemical energy storage systems. *Applied Energy, 254*, 113733. https://doi.org/10.1016/j.apenergy.2019.113733

Tinkham, M. (2004). Introduction to Superconductivity. Courier Corporation.

Topal, U. & Akdogan, M. (2012). The Role of Oxygenation on Superconducting Properties of RE3Ba5Cu8O18 (RE=Y, Sm and Nd) Compounds. *Journal of Superconductivity and Novel Magnetism, 25*(2), 239-244. https://doi.org/10.1007/s10948-011-1285-3

van Otterlo, A., Golubev, D. S., Zaikin, A. D., Blatter, G. (1999). Dynamics and effective actions of BCS superconductors. *The European Physical Journal B - Condensed Matter and Complex Systems, 10*(1), 131-143. https://doi.org/10.1007/s100510050836

Vidal, F., Viera, J. A., Maza, J., Ponte, J. J., García-Alvarado, F., Morán, E., Amador, J., Cascales, C., Castro, A., Casais, M. T., Rasines, I. (1988). Excess electrical conductivity in polycrystalline Bi-Ca-Sr-Cu-O compounds and thermodynamic fluctuations of the amplitude of the superconducting order parameter. *Physica C: Superconductivity, 156*(5), 807-816. https://doi.org/10.1016/0921-4534(88)90166-9

Wang, Y., Ono, S., Onose, Y., Gu, G., Ando, Y., Tokura, Y., Uchida, S., Ong, N.P. (2003). Dependence of upper critical field and pairing strength on doping in cuprates. *Science, 299*(5603), 86-9. https://doi.org/10.1126/science.1078422

Wang, Y., Zhang, Z., Gao, Z., Wang, L., Wang, Q. (2025). Effect of oxygen partial pressure on the preparation of phase-pure YbBa2Cu3O7-y superconductor by solid-state sintering method. J*ournal of the European Ceramic Society, 45*(10), 117325. https://doi.org/10.1016/j.jeurceramsoc.2025.117325

Yamamoto, A., Polyanskii, A. A., Jiang, J., Kametani, F., Tarantini, C., Hunte, F., Jaroszynski, J., Hellstrom, E. E., Lee, P. J., Gurevich, A., Larbalestier, D. C., Ren, Z. A., Yang, J., Dong, X. L., Lu, W., Zhao, Z. X. (2008). Evidence for two distinct scales of current flow in polycrystalline Sm and Nd iron oxypnictides. *Superconductor Science and Technology, 21*(9), 095008. https://doi.org/10.1088/0953-2048/21/9/095008

Zhang, Y. & Xu, X. (2020). Yttrium barium copper oxide superconducting transition temperature modeling through gaussian process regression. *Computational Materials Science, 179*, 109583. https://doi.org/10.1016/j.commatsci.2020.109583

Ziemke, C.D., Nguyen, H-M., Amaya-Roncancio, S., Gahl, J., Xing, Y., Heitmann, T.W., Wexler, C. (2025). Formation of lattice vacancies and their effects on lithium-ion transport in LiBO2 crystals: Comparative ab initio studies. *Journal of Materials Chemistry A, 13*, 3146-3162. https://doi.org/10.1039/D4TA05713A